CHAPTER V
NGC 4254 – a case study

Based on: “Probing for dark matter in spiral galaxy disks”
Kranz, Slyz & Rix 2001, ApJ, 562, 164

We[1] selected NGC 4254 (Messier 99) as the first galaxy from our sample to be analyzed, because it shows a clear spiral structure with high arm-inter-arm contrast. NGC 4254 is a bright Sc I galaxy located in the Virgo galaxy cluster with a recession velocity of $2453\,\mathrm{km\,s^{-1}}$ adopted from the SIMBAD database. We assume a distance of 20 Mpc towards NGC 4254, taken from the literature (Sandage & Tammann 1976; Pierce & Tully 1988; Federspiel, Tammann & Sandage 1998). It has a total blue magnitude of $B_T = 10.2$ and a diameter of 5.4×4.7 arcmin on the sky. At 20 Mpc one arc second is 97 parsecs in the galaxy which translates to 38.4 pc per detector pixel. Our Hα rotation curve for NGC 4254 (see Figure 4.5) rises steeply out to $\sim 35''$ (3.4 kpc) and then flattens at a rotation velocity of $\sim 155\,\mathrm{km\,s^{-1}}$. This agrees well with earlier estimates (Phookun, Vogel & Mundy 1993). From the kinematics we know that the south-western part of the galaxy is approaching. If we assume trailing spiral arms then the galaxy rotates clockwise when viewed from our perspective.

In the K-band NGC 4254 shows very prominent two-arm spiral features at most radii. The northern arm bifurcates at R $\approx$ 4.5 kpc, causing a three arm pattern in the outer disk. Furthermore, the galaxy exhibits considerable lopsidedness. NGC 4254 shows a strong arm-interarm brightness contrast, noted by Schweizer (1976) to be even stronger than the one for NGC 5194 (M 51). Even in the K-band the brightness contrast is rather high, more than one magnitude over a wide radial range. González & Graham (1996) argued that, combined with a usual density wave, some external mechanism is needed to invoke such high contrasts. However, NGC 4254 is well separated from any other galaxy in the cluster. Phookun, Vogel & Mundy (1993) reported in their paper the detection of high velocity H I clouds outside the disk's H I emission. The authors argue that in-falling H I gas may be responsible for the unusual ”one armed” outer structure of the spiral. In that case the spiral structure of NGC 4254 may have been recently reorganized, enhancing the southern arm or the arm-interarm mass density distribution. Recent interactions could in principle corrupt the project's assumption of a steady state spiral pattern. But as we will find from our full analysis, the steady state assumption is seemingly not far off on time scales of a few dynamical periods.

NGC 4254 harbors a small bar-like structure at its center with a major axis position angle of $\approx 40°$(see Figure 5.1a). From both ends of the bar two major arms emerge with a third

[1]The use of plural emerges from the fact, that the content of this Chapter was partially copied from a multi-author paper.

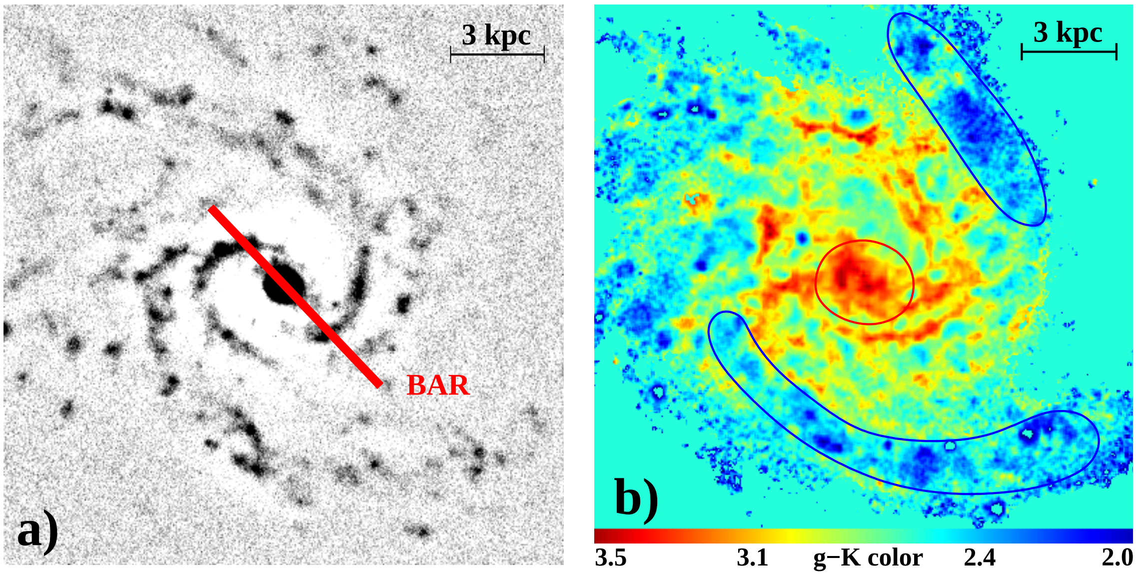

Figure 5.1 Properties of NGC 4254. Panel **a)** shows the morphology and the position of the small bar. The image has been treated with the unsharp mask subtraction technique to enhance the spiral features. **b)** shows the $g - K$ color map of NGC 4254. The bulge exhibits a redder color while the spiral arms appear bluer (circled areas).

arm splitting off the northern arm. By analyzing a $g - K$ color map of NGC 4254 one learns that this third arm, together with the southern strong arm, is significantly bluer than the other regions of the galaxy and thus consists of a younger stellar population. The inner small bulge appears red in the color map (see Figure 5.1b).

In the K-band the disk of NGC 4254 is well approximated by an exponential with a scale length of $\mathrm{R_{exp}} \approx 36''$, corresponding to ≈ 3.5 kpc if a brightness average of the arm and interarm regions is considered and bright H II regions are removed from the image. Except for the very center, the whole surface brightness profile is well fitted by a double exponential model with an inner 'bulge' scale length of ≈ 0.6 kpc.

5.1. Hydrodynamic simulations for NGC 4254

To model the two-dimensional gas surface densities and velocity fields for NGC 4254 we carried out a set of simulations on a 201 by 201 evenly spaced Cartesian grid. Our data for NGC 4254 extend out to a radius of about 11.6 kpc, hence on a 201 by 201 grid this gives a resolution of about 116 pc per side of a grid cell, which is considerably higher than the effective force smoothing of 400 pc.

The gas temperature profile is taken to be uniform and by imposing an isothermal equation of state throughout the simulation we assume that the gas instantaneously cools to its initial temperature during each updating timestep. The initial density profile of the gas is exponential with a scale length equal to a third of the disk radius, namely 3.86 kpc. We begin each simulation with the gas initially in inviscid centrifugal equilibrium in the axisymmetric potential given by $\Phi_{\star,\mathrm{ax}}$ and Φ_{halo} (see Section 4.1.5). Following the initial-

Table 5.1 Dark halo parameters.

$\mathrm{f_d}$ (M_D/M_{Dmax})	R_c (kpc)	v_∞ ($\mathrm{km\,s^{-1}}$)	χ^2/N
0.2	1.08	155	2.45
0.4444	2.00	150	3.42
0.6	3.03	150	3.30
0.85	5.68	155	2.00
1.0	7.30	155	1.84

Note: Dark halo parameters used to generate the potentials used for simulations. The χ^2/N-values refer to an axisymmetric model.

ization of the gas in centrifugal balance, we slowly turn on the non-axisymmetric potential at a linear rate computed by interpolating between the final non-axisymmetric potential and the initial axisymmetric potential so that the potential is fully turned on by the time 40 sound crossing times of the code have passed. Here the sound crossing time is defined as the time it takes to traverse the length of the diagonal of a grid cell at sound speed. For an isothermal simulation with a sound speed of $10\,\mathrm{km\,s^{-1}}$ the sound crossing time of a cell in our simulation is about 16 Myr, so that by 40 sound crossing times, the gas has evolved for 640 Myr which is about 1.4 times the dynamical time of the galaxy measured at a radius of 11.6 kpc. After the non-axisymmetric part of the gravitational potential has been fully turned on, we continue to run the simulation for about another dynamical time.

We ran a large set of simulations both to understand the power and limitation of our modelling in general and to match the observations. Simulations were performed for a total of five different fractions $\mathrm{f_d}$ of the stellar disk: disk only, i.e. $\mathrm{f_d} = 1$, and $\mathrm{f_d} = 0.85$, 0.6, 0.4444 and 0.2, or accordingly $\mathrm{f_d}$ is given in percent from 20 % to 100 %. In all the cases the core radius and the asymptotic velocity of the pseudo-isothermal halo were adjusted to best match the averaged rotation curve, as summarized in Table 5.1. The variations in χ^2/N between the low mass disks and the massive ones are mainly caused by the attempt to keep R_c and v_∞ at physically reasonable values. The bump at $20''$ to $40''$ (Figure 4.5) is fitted better for the high mass disks, which reduces the overall χ^2 compared to the low mass disks.

We have no secure prior knowledge of the spiral pattern speed Ω_p. We determine it by assuming different values for Ω_p and then comparing a simulation to the data. For every simulation with a different stellar/dark halo combination, we get slightly different values for the best matching Ω_p or equivalently for the corotation radius R_CR. We covered the complete range of reasonable R_CR, i.e. from about a disk scale length to well outside the disk. We even made simulations for the case of no spiral pattern rotation, $R_\mathrm{CR} \to \infty$.

To test how the amplitude of the velocity perturbations depends on the responsiveness of the gas, we ran simulations at a variety of temperatures corresponding to sound speeds c_s, of 10, 15, 20 and $30\,\mathrm{km\,s^{-1}}$. In the following Sections we discuss some of the results from the simulations.

5.2. Results for NGC 4254

5.2.1. Simulated Gas Density

Figure 5.2 shows eight views of the simulated gas density for different pattern speeds overplotted as contours over the deprojected, color corrected K-band image of NGC 4254. The simulated gas density follows an overall exponential profile with a scale length of $\approx 4.2\,\mathrm{kpc}$, comparable to the one of the disk itself. The contours in the Figure are chosen to highlight the density enhancements and locations of the gas shocks caused by the spiral arms. For almost all simulated cases the strong part of the galaxy's spiral structure lies well inside corotation, where the circular velocity is larger than the spiral pattern speed. The gas will thus enter the spiral arms from their inward facing side, producing the strongest shocks there. For a well matching simulation, we expect the shocks to be near the OB associations that trace the spiral arms.

It is remarkable how well the overall morphology of NGC 4254 can be matched by the gas density simulations. Not only are the two major spiral arms clearly identifiable in most simulations but the less prominent northern arm and the locations where the arms bifurcate are reproduced in some cases well. For fast pattern speeds ($R_{\mathrm{CR}} = 5.4 - 7.58\,\mathrm{kpc}$ in Figure 5.2) we find a strong shock in the northern part of the galaxy that cannot be correlated with any mass feature. We believe it develops because the potential close to the upper boundaries of the computational grid is quite non-axisymmetric, and this leads to a spurious enhancement of a shock. The shock does not propagate into regions inside the corotation radius, and therefore we refrain from smoothing the potential.

It is important to note that the simulations lead to a very stable gas density distribution that does not change much after the non-axisymmetric potential is fully turned on. When the contribution of the disk is increased in the combined potential, all spiral features get enhanced in the gas density but the galaxy morphology is essentially unchanged. With increasing pattern rotation (smaller corotation radii in Figure 5.2) we find that the predicted spiral arms become more and more tightly wound. For a comparison to the stellar spiral morphology we need to define some criteria to pick the right model. If the situation in NGC 4254 is similar to NGC 4321, whose gas and dust distributions and their connection to star forming regions have been discussed in detail by Knapen & Beckman (1996), then a good matching gas morphology is one where for radii smaller than the corotation radius, the shocks in the gas density lie on the inside of the stellar spirals. Shortly downstream from there, many star forming H II regions, triggered by gas compressions, should show up as patches in the arms. According to these criteria, the best matching morphology can be unambiguously identified to be produced by a simulation with $R_{\mathrm{CR}} \approx 7.6\,\mathrm{kpc}$ (Figure 5.2 upper right panel), corresponding to a pattern speed of $\Omega_{\mathrm{p}} \approx 20\,\mathrm{km\,s^{-1}kpc^{-1}}$. $R_{\mathrm{CR}} = 6.4\,\mathrm{kpc}$ and $R_{\mathrm{CR}} = 8.3\,\mathrm{kpc}$ enclose the range of possible values. This corresponds to an uncertainty of $\sim$ 15% in the value of R_{CR}.

Our results were compared to values of R_{CR} for NGC 4254 from the literature, which were determined by different means. The results $R_{\mathrm{CR}} \sim 8.45\,\mathrm{kpc}$ (Elmegreen et al. 1992) and $R_{\mathrm{CR}} = 10.2 \pm 0.8\,\mathrm{kpc}$ (González & Graham 1996), scaled to our distance assumptions, provide larger estimates than ours. However, given the picture of non-linear orbital models, where the strong part of the stellar spiral is expected to end inside the inner 4/1 resonance

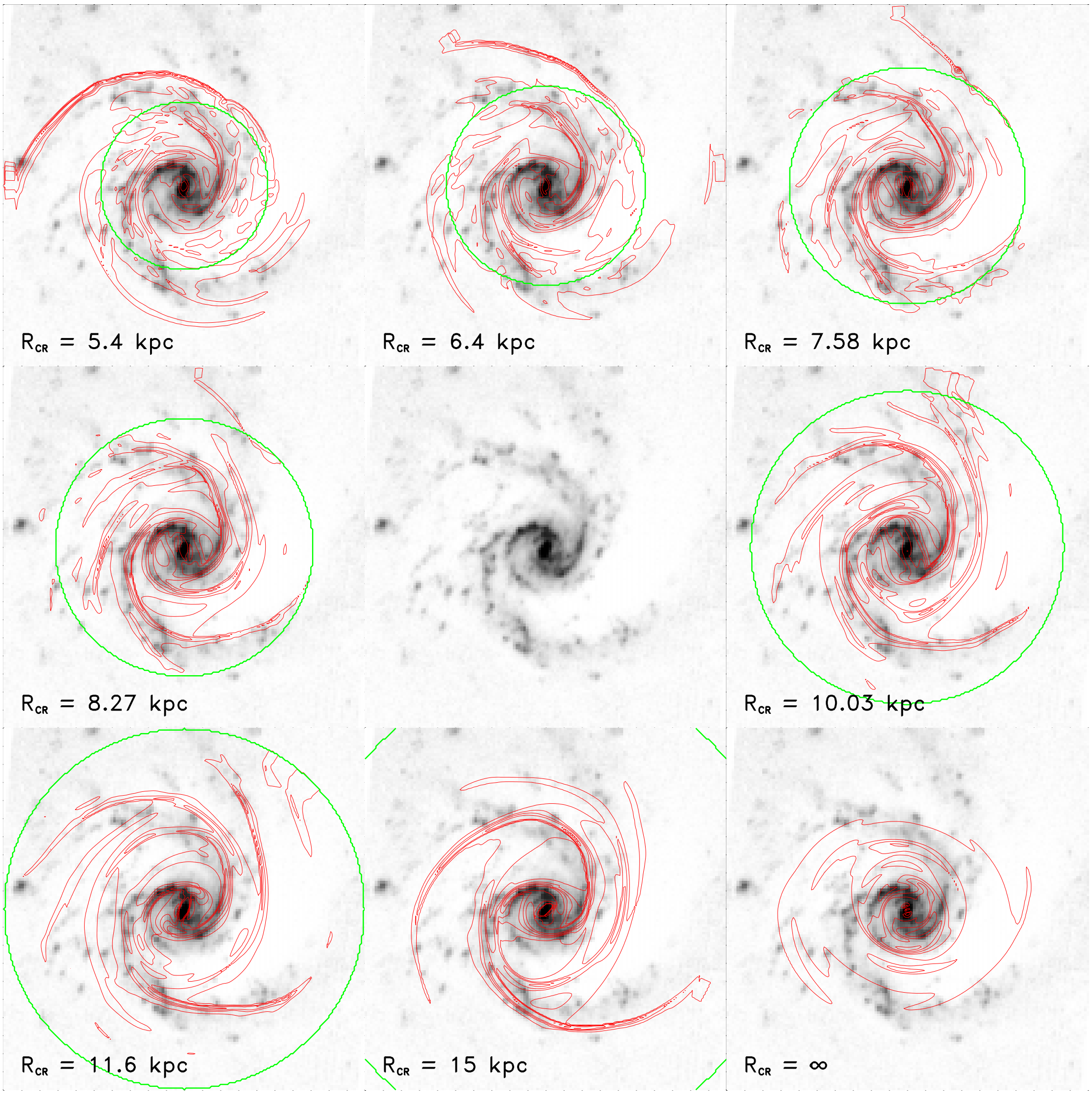

Figure 5.2 Simulation results of the gas density distribution over-plotted in red contours on the deprojected K'-band image of NGC 4254 (center). From the image an axisymmetric radial brightness profile has been subtracted to enhance the contrast of the spiral arms. The results are displayed for eight different assumptions for the pattern speed, respectively the corotation radius R_{CR}. The green circle marks corotation. The range goes from fast rotation $R_{\mathrm{CR}} = 5.4$ kpc to slow pattern rotation $R_{\mathrm{CR}} = 15$ kpc, lying mostly outside the image frame and finally for no pattern rotation. Displayed are the results from the $\mathrm{f_d} = 60\,\%$ case.

(Patsis et al. 1991) we find that $R_{\mathrm{CR}} \approx 7.6$ kpc is consistent with the galaxy's morphology. In short, these simulated gas densities provide us with an excellent tool to determine the pattern rotation speed of the galaxy. Apart from requiring a constant global pattern rotation our approach is independent of an underlying spiral density wave model. The overall very good representation of the whole spiral structure by the simulated gas density makes us rather confident that the simulations render realistic processes affecting the gas.

5.2.2. Simulated Gas Velocity Fields

As another output of our simulations we get the two-dimensional velocity field of the gas. As is evident from a comparison to the gas density distribution, the velocity jumps are – as expected – at the locations where the density map shows the shocks. They show up as areas of lower local circular velocity compared to the elsewhere rather smoothly varying gas velocity field. The velocity wiggles, as well as the density shocks themselves, have very tight profiles and thus are even more narrow than the physical extent of the stellar arms. They have to be compared to the observed kinematics.

5.2.2.1. The observed kinematics

The rotation curves at the 16 slit positions from the observations are shown in Figure 5.3 as data points. It is apparent that the longslit spectra allow a good velocity coverage along the slits. Almost all rotation curves show contiguous data points out to a radius of $\gtrsim 1\farcm5$. The spectra exhibit a lot of wiggles on a small spatial scale. Jumps of $\lesssim 30\,\mathrm{km\,s^{-1}}$ on a scale of $\sim 5''$ are common. The very prominent jumps that we observed in slit positions $22\fdg5$ and $225°$ clearly exceed the average wiggle sizes. Inside of about $0\farcm3$ the small bar influences the velocity field. The most prominent trace of the bar occurs at its minor axis at the slit positions of $135°/157\fdg5$ and $315°/337\fdg5$.

The trace of kinematic features in the outer disk is not conspicuous in subsequent slits. The eastern part of the disk (slit positions $45° - 135°$) displays a quite smooth velocity field, while the western part shows some large scale variations. Aside from the inter-arm region between the inner disk and the southern arm where a $\approx 0\farcm5$ wide depression is moving outward in subsequent slits (positions $\geq 247\fdg5$) no significant features are apparent in the outer disk. Unfortunately in this inter-arm region the S/N is not so good. Does that mean we do not see the trace of the arms in the velocity field, or is the single slit representation of the 2D velocity field misleading and does not allow us to identify coherent features in adjacent slits? Clearly, the wiggles associated with spiral arms in NGC 4254 are not nearly as strong as in M 81 (Visser 1980), thus their identification is harder. A CO map of NGC 4254's center (Sakamoto et al. 1999) shows also no coherent wiggles across spiral arms and we doubt that it would be much different on a Fabry-Perot image. Rather than being confused by the one dimensional nature of our rotation curve slices we believe that the spiral features in the velocity field are intrinsically weak.

5.2.2.2. Overall Fit Quality

Figure 5.3 shows the 16 separate rotation curves with a corresponding simulated velocity field over-plotted. The simulation used here for comparison is the one for which the gas density distribution best-fit the K-band image (displayed in Figure 5.2). It has a corotation radius of $R_{\mathrm{CR}} = 7.58\,\mathrm{kpc}$ – corresponding to a pattern speed of $\Omega_{\mathrm{p}} = 20\,\mathrm{km\,s^{-1}kpc^{-1}}$ – and a stellar disk mass fraction $\mathrm{f_d}$ of 60 %. A gas sound speed of $c_s = 10\,\mathrm{km\,s^{-1}}$ was assumed here.

The general fit quality is governed by the effect that the projection of the simulated velocity field introduces. The good overall match indicates that we quite reliably found the right position angle and inclination for the galaxy. The simulated velocities align very well with the measured data points. In addition to the good overall match, the general

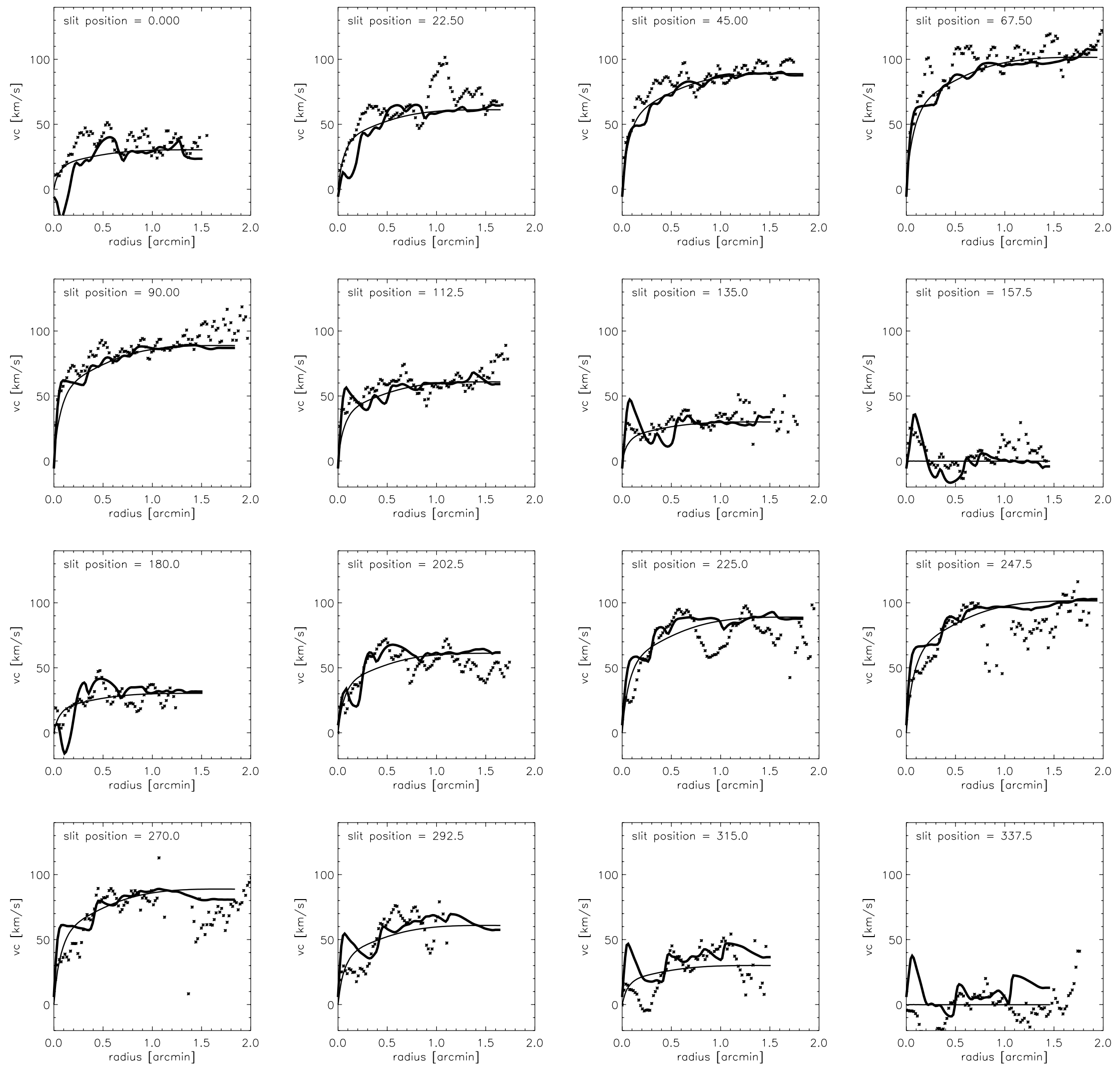

Figure 5.3 Simulation results of the gas velocity field in comparison to the observed rotation curves. Displayed are the measured rotation curves (data points), the axisymmetric model (thin line) and the rotation curves from the hydrodynamical simulations (thick line) for all 16 slit position angles. The parameters for the simulation were: f_d of 60 % and $R_{CR} = 7.58$ kpc. There are no error bars plotted for the data, but the errors can be estimated from the point-to-point scatter of the data.

rising or falling shape of the separate curves is also excellently reproduced by the simulations. The lopsidedness of the galaxy is reflected in the shape of the rotation curves on the receding and approaching side of the disk. At the receding side ($67\overset{\circ}{.}5$) the rotation curve rises steeply and continues to rise out to $2'$, while the approaching side ($247\overset{\circ}{.}5$) rises less steeply but flattens out or even drops beyond $0\overset{\prime}{.}7$. These characteristics are closely reproduced by the models.

A close inspection of the two profiles shows however that the overlap in the match of the simulated velocities with the measurements is not always satisfactory. The agreement of local features in the simulations and the measured data is sometimes very good and

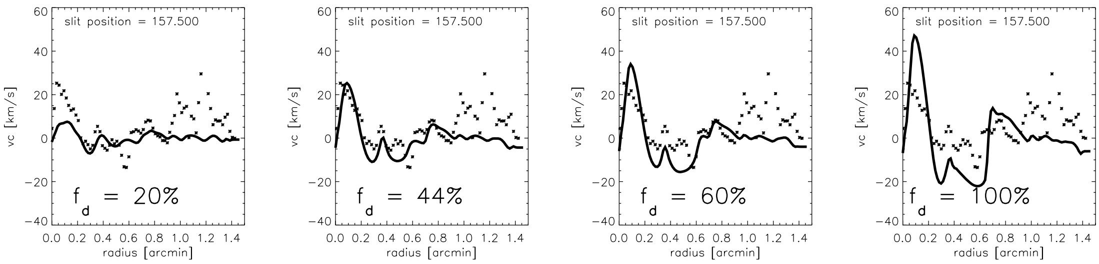

Figure 5.4 Comparison of four simulations for different fractions f_d of the stellar mass component. The simulation was done with a corotation radius of 7.58 kpc and a gas sound speed of $10\,\mathrm{km\,s^{-1}}$. Displayed is one of the 16 slit positions. Clearly the predicted "wiggles" in the rotation curve grow much stronger for higher disk mass fractions.

even occurs in subsequent slit positions. However, there are also many locations, where the match is poor. This is particularly the case in the inner region of the galaxy, where the small bar dominates the kinematics. Both profiles show strong wiggles where the slit crosses the bar, especially close to the minor axis of NGC 4254's velocity field, which is also close to the minor axis of the bar itself. While the simulations show a rather symmetric imprint, the measurements exhibit a signature different from that, leading to a significant mismatch at several slit positions, e.g., 292°.5 and 337°.5. This might be caused by the bar, having a slightly different pattern speed. In the outer parts of the rotation curve we also find several wiggles in the observed data that have no correspondence to the wiggles in the simulations and vice versa. It is important to note that we do not expect to reproduce all the wiggles in the galaxy's rotation curves, since we are only modelling those created by the non-axisymmetric gravitational potential. The wiggles originating for another reason – like expanding SN gas shells – are not considered by the simulations and thus do not show up in the resulting velocity field.

An overall fit quality gets determined by a global χ^2-comparison of the simulated velocity field to the actual observed velocity field along the 16 measured slit positions. The χ^2-fitting excludes the very central region hosting the small bar because the modelling is not intended to fit the central bar, which might have a different pattern speed. The total number of data points included in the χ^2-fitting is 1077.

5.2.2.3. Varying the Stellar to Dark Matter Ratio

As already mentioned in Section 5.1, we performed simulations for five stellar disk and dark halo combinations, as listed in Table 5.1. Since the non-axisymmetric perturbations are induced in the potential by the stellar contribution, we expect the amplitude of the wiggles in the modelled rotation curves to depend significantly on the non-axisymmetric contribution of the stellar potential whereas we expect the radial distribution of the wiggles to be rather independent of the stellar mass fraction. As expected, in the simulations with the lightest disk, the wiggles look like modulations on the axisymmetric rotation curve. In the case of the maximum disk, the rotation curves are strongly non-axisymmetric (see Figure 5.4). This is also very evident from Figure 5.5, which shows the log of the gas density for the sequence of simulations. The density contrast between high and low density regions increases dramatically as the disk fraction increases. To describe this characteristic more quantitatively, we learn from Figure 5.6 that the amplitude of the deviations from axisymmetry increases linearly with the mass fraction of the stellar disk, which proves the general validity of the concept with which we try to approach this problem.

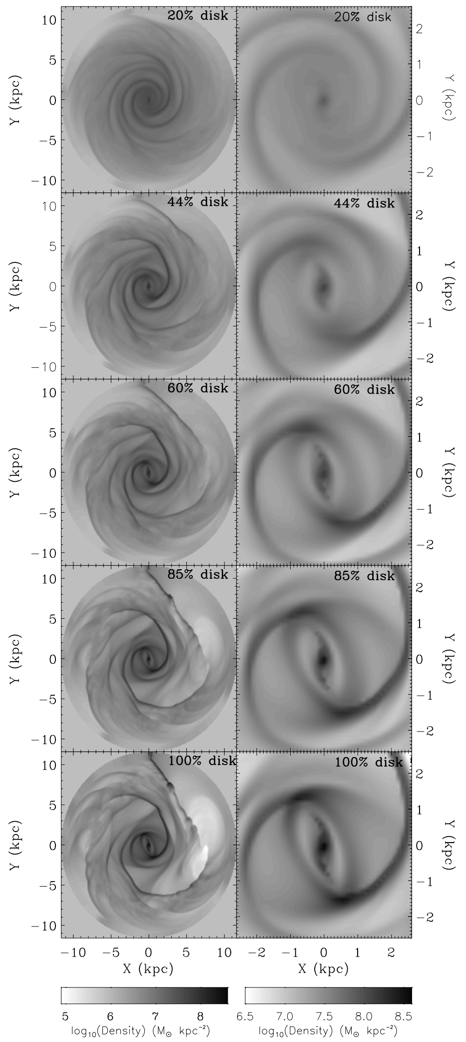

Figure 5.5 Grey scaled maps of the log of the density from simulations on a 201×201 grid, with $c_s = 10\,\mathrm{km\,s^{-1}}$, and $R_{\mathrm{CR}} = 7.58\,\mathrm{kpc}$, and with increasing disk contribution to the total galactic potential. The left column shows the entire simulated region, and the right column shows only the inner $2.6\,\mathrm{kpc}^2$ region.

For the lowest disk fraction case (20 % disk), we find that the spiral arms are most tightly wound and most smooth in their curvature. Increasing the disk fraction to 44 %, also increases the pitch angle of the spiral arms. The overall morphology of the structure appearing over the full disk (11.6^2 kpc) is mostly unchanged once the disk fraction is 44 % and higher. There are slight differences in the details. As seen further from the right column of Figure 5.5, the barred structure in the central region also grows stronger. In fact, the strongest velocity wiggles arising in the modelled velocity fields are the ones connected to the central bar-like feature. However, since here we are not interested in modelling the dynamics of the bar, we exclude this inner part from the analysis. If we do a formal χ^2 comparison of the models with the observed data we find that for most of the sub-maximal disks the fit is considerably better than for heavy stellar disks. By formal, we mean that we use all data points for the χ^2-fit, regardless of whether a certain part matches well or not with two exceptions: we exclude the very central part with the bar and we correct for the outer strong shock appearing in the fast rotating models (see Figure 5.2).

The result from this χ^2-fit is presented in Figure 5.7. In all cases, $\mathrm{f_d} = 100\,\%$ gives the worst fit to the observed rotation curves. For the lower mass disks it is very hard to decide, whether a particular disk mass is preferred. For $R_{\mathrm{CR}} = 6.4\,\mathrm{kpc}$ we find about the same χ^2 for all non-maximal disk models. Since we can not reject data on a physical basis, we can state only a trend at this point. Thus, our conclusion from this part of the analysis is that the disk is most likely less than 85 % maximal.

One very interesting thing to mention is the fact that the formally preferred axisymmetric maximum-disk decomposition (see Table 5.1) turns out to be the most unfavored model, once the simulations were performed. This implies that even if an axisymmetric model

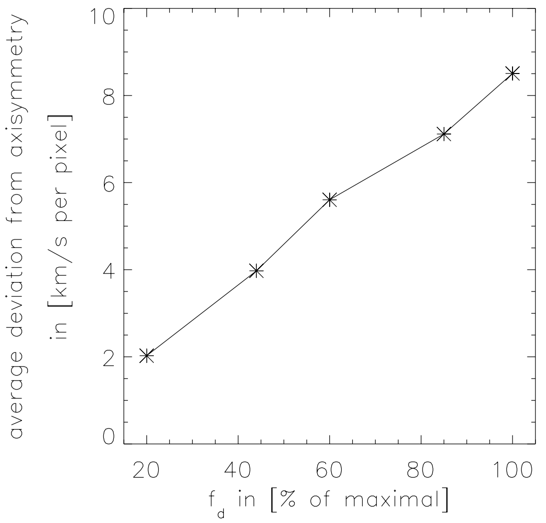

Figure 5.6 Deviation of the simulation from axisymmetry. Displayed is the average deviation of each radial simulation bin from the axisymmetric rotation curve. It rises linearly with the stellar disk mass contribution f_d.

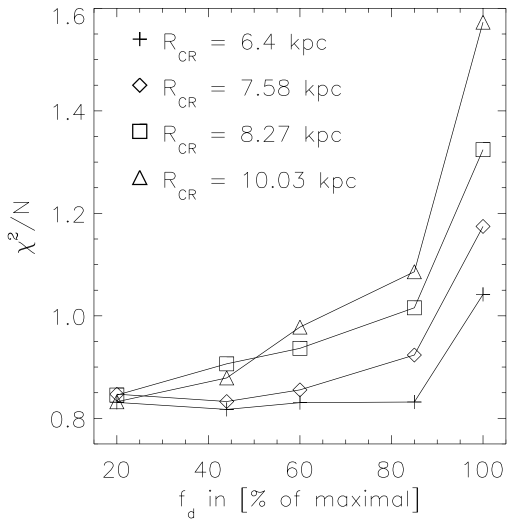

Figure 5.7 Formal χ^2-fit of the gas velocity simulations for different stellar mass contributions f_d, normalized by the χ^2-fit for the axisymmetric model rotation curve. Displayed are cases for four different values of R_{CR}. From the simulations we can rule out the cases with the highest disk mass.

profile provides a better fit to a measured rotation curve, it does not necessarily mean, that this combination provides the best fit when one considers the 2D non-axisymmetric gas evolution.

5.2.2.4. Varying the Gas Temperature

This kind of analysis may be very sensitive to the temperature of the gas which is assumed for the modelling. Higher gas temperature corresponds to a higher cloud velocity dispersion c_s and thus to a reduction in the response of the gas to any feature in the gravitational potential.

Within the Milky Way Galaxy c_s varies from $\approx 6\,\mathrm{km\,s^{-1}}$ in the solar neighborhood to $\approx 25\,\mathrm{km\,s^{-1}}$ in the Galactic center (Englmaier & Gerhard 1999). For simulations of a galactic disk with an isothermal equation of state, the most commonly used values for c_s are 8 – $10\,\mathrm{km\,s^{-1}}$, corresponding to $< 10^4\,\mathrm{K}$ in gas temperature (Englmaier & Gerhard 1999; Weiner et al. 2001a). In these simulations the authors make the statement that within the reasonable limits of $c_s = 5 - 30\,\mathrm{km\,s^{-1}}$ the modelled gas flows across the primary shocks is not considerably affected.

Only when modelling strong bars in galaxies the simulations might be dependent on the choice of the gas sound speed (Englmaier & Gerhard 1997). For the main set of simulations we chose $c_s = 10\,\mathrm{km\,s^{-1}}$, corresponding to a gas temperature of 7250 K. To probe the effect of the gas temperature, we performed simulations for four different gas sound speeds, c_s, of 10, 15, 20 and $30\,\mathrm{km\,s^{-1}}$. The resulting gas density distributions for the high resolution

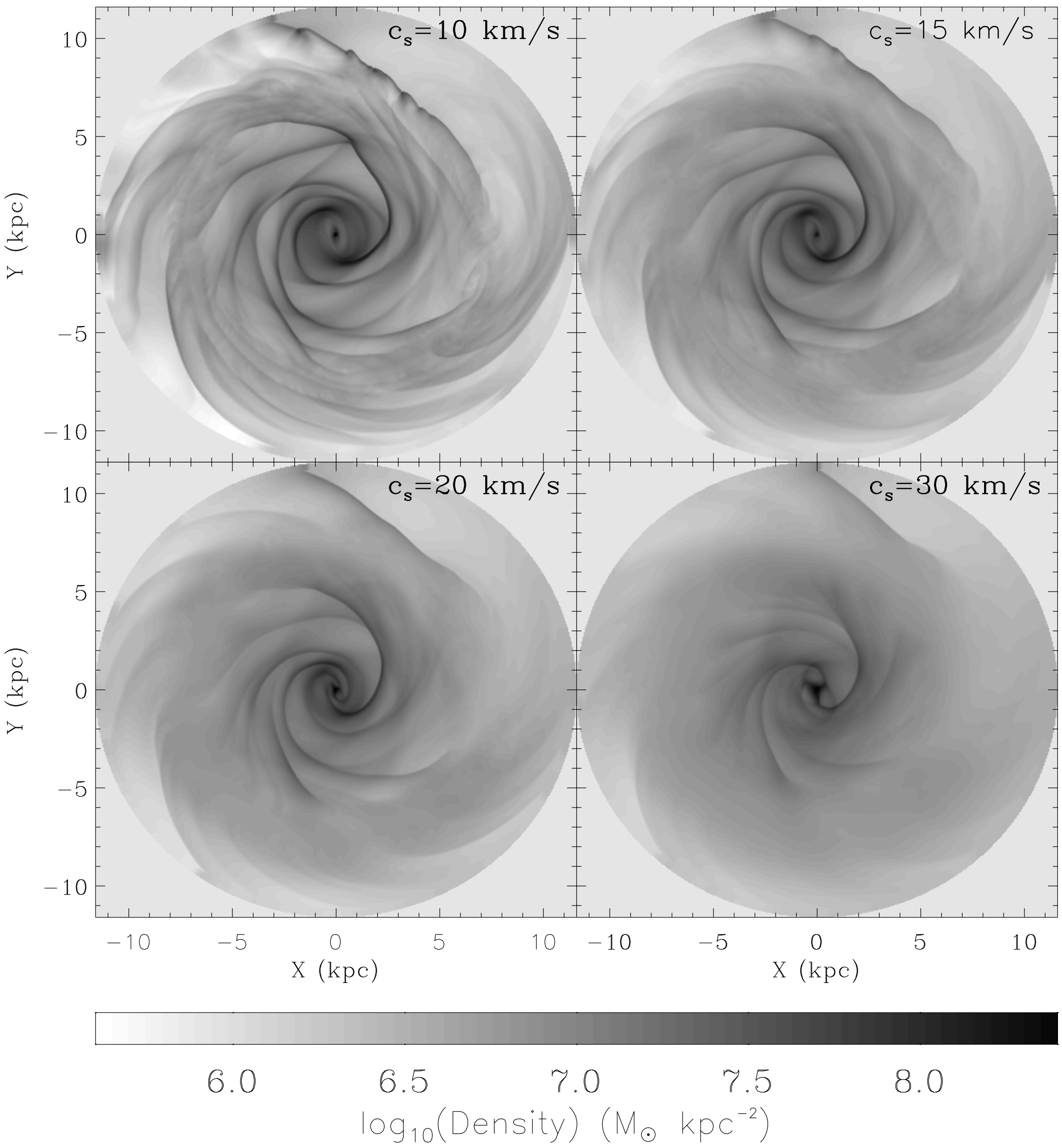

Figure 5.8 Grey scaled maps of the log of the gas density from simulations on a 401×401 grid, with 60 % disk fraction, $R_c = 7.58$ kpc. Four cases are displayed with increasing sound speed c_s, of 10, 15, 20 and $30\,\mathrm{km\,s^{-1}}$. The entire simulated region is shown.

simulation are displayed in Figure 5.8. Since at higher sound speeds the pressure of the gas becomes more important, the gas responds less strongly to the stellar density wave forcing. This is obvious when one looks at figure 5.8 where in a sequence of simulations differing only in their sound speed we see the non-axisymmetric features in the gas gradually fade with increasing sound speed. By $c_s = 30\,\mathrm{km\,s^{-1}}$ the spiral structure does not extend as far as it does in the colder gas cases even though there are still traces of some of the major spiral features. However, a sound speed of $c_s = 30\,\mathrm{km\,s^{-1}}$ implies a gas temperature of ≈ 65.000 K for a monatomic ideal gas. This is an extreme test case that does not apply to real galaxies. Furthermore, the strength of the wiggles in the velocity field vary only very little between $c_s = 10 - 20\,\mathrm{km\,s^{-1}}$. We conclude that varying the value for c_s within reasonable limits, the morphology and velocity fields of the simulations are affected not enough to change the conclusions for this galaxy.

5.2.2.5. Varying the Grid Resolution

The choice of the grid size was mainly motivated by the desire to achieve reasonable computing times, and not to exceed the seeing resolution. To check the grid cell size's effect on the results, for selected cases we also ran simulations on grids with two times higher resolution, 401×401 cells, as well as on grids with two times lower resolution on a 101×101 grid.
Decreasing the grid resolution increases the numerical diffusivity of the code. One reason for this is that on a coarser grid one stores hydrodynamical information in larger cells, meaning that information is averaged over larger areas, thus causing loss of information on finer scales. Figure 5.9 shows how the shock transitions are increasingly blurred on coarser grids. Many features in the density map that appear for the 201×201 and the 401×401 grids are not present at all on the 101×101 map. The morphology of the 201×201 map on the other hand, is very similar to the 401×401 grid.

The final χ^2-fit deviation between simulations with different grid cells ranges at about 6 % and does not change the conclusions of this paper. Accordingly we consider it safe to perform the simulations on the medium resolution grid we used.

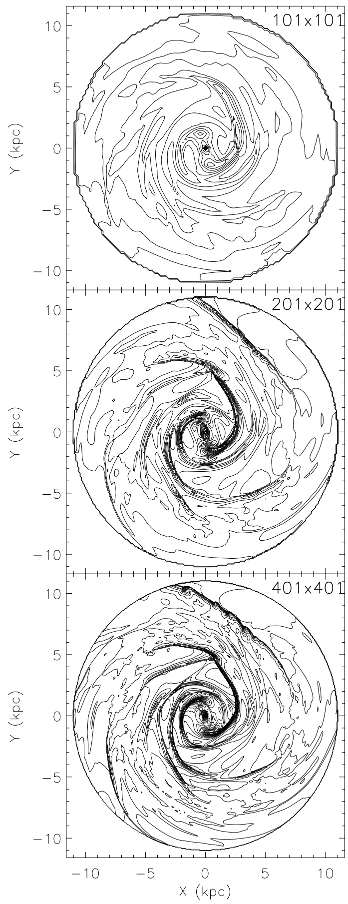

Figure 5.9 Contour maps of the density from simulations with $c_s = 10\,\mathrm{km\,s^{-1}}$, 60 % disk fraction, $R_{\mathrm{CR}} = 7.58\,\mathrm{kpc}$, and with increasing grid resolution. The full potential is turned on in 20 cell sound crossing times for the 101×101 grid, 40 t_s for the 201×201 grid, and 80 t_s for the 401×401 grid. The result is shown after 1590 Myr (t_{dyn}) have elapsed.

5.3. Discussion of possible caveats

A comparison of the observed and simulated kinematics has turned out to be challenging. Although the overall shapes of the different rotation curves were very well reproduced by the simulations, some small scale structure remains unmatched. The formal comparison of the gas velocity field to the observed Hα kinematics favors simulations with small disk mass fractions $\mathrm{f_d}$ (see Figure 5.7) and correspondingly small values for the stellar mass-to-light ratio. With the K-band mass-to-light ratio discussed in Section 4.1.5 our results yield an overall stellar M/L of $\Upsilon_\star \lesssim 0.5$. We can estimate the relative mass fractions from their contributions to the total rotation velocity. At a radius of 2.2 uncorrected K'-band exponential disk scale lengths

($2.2\,R_{\rm exp} \approx 79''$ or $7.7\,$kpc), the individual rotational support of the stellar and dark halo components for $\rm f_d = 85\,\%$ are $v_\star = 125\,{\rm km\,s^{-1}}$ and $v_{\rm halo} = 86\,{\rm km\,s^{-1}}$. If a total mass is estimated via

$$\mathrm{M}(2.2R_{\rm exp}) = \frac{v^2(2.2R_{\rm exp}) \times 2.2R_{\rm exp}}{G} \tag{5.1}$$

we find that $M_{\rm halo} \approx 0.47\,M_\star$ at $R = 2.2\,R_{\rm exp}$, or accordingly $\gtrsim 1/3$ of the total mass inside $R_{\rm exp}$ is dark. Since our confidence limits are not very tight, we cannot use them to test other authors' findings in detail. Projects yielding results in favor of a sub-maximal stellar disk usually find a disk mass fraction less than our upper limit estimate. Bottema (1997) as well as Courteau & Rix (1999) conclude that the contribution of the stellar disk to the total rotation is $v_\star \sim 0.6\,v_{\rm tot}$ which translates to $M_{\rm halo} \sim 0.6\,M_{\rm tot}$. At the current state of the project we cannot exclude or confirm these findings. This issue is going to be discussed more thoroughly as soon as we have a few more examples analyzed.

In the following Sections we will discuss the details that could cause deviations from a perfect match between the simulations and the measurements.

5.3.1. Is the Concept Reasonable?

If the self-gravity of the stellar mass in the disks of spiral galaxies plays an important role then undoubtedly the potential becomes non-axisymmetric. The trajectory of any kinematic tracer in the galaxy, such as the gas, should be affected by these potential modulations. But is the H II component of the gas the best choice for tracing the galaxy's potential? Analytic calculations of gas shocks in the gravitational potential of a spiral galaxy (Roberts 1969) tell us that we should expect velocity wiggles with an amplitude of 10 to $30\,{\rm km\,s^{-1}}$ while crossing massive spiral arms. However, kinematic feedback to the gas from regions of massive star formation, from expanding gas shells produced by supernova explosions and from other sources of turbulence, introduces small-scale random noise in the velocity fields. These fluctuations typically lie in the range of 10 to $15\,{\rm km\,s^{-1}}$ (Beauvais & Bothun 1999) and seem even higher in the case of NGC 4254. The kinematic small-scale noise could be increased if the dynamics of the brightest H II regions is kinematically decoupled from the global ionized gas distribution. To check this we over-plotted the Hα-intensity on the rotation curves to see if the star formation regions coincide with the strongest wiggles in the rotation curves. There is, however, no discernible relation between the amplitude of a wiggle and the intensity of the H II region, indicating that the deviations are not confined to compact H II regions (see Figure 5.10).

As an alternative to observing the ionized phase of the hydrogen gas, one could consider using H I radio observations. However, available H I data are limited by the larger size of the radio beam that smears out kinematic small-scale structures in the gas. In principle, stellar absorption spectra could also provide relevant kinematic information, but this approach has two disadvantages compared to an approach using gas kinematics. First, the acquisition of stellar absorption spectra with sufficient S/N would take a prohibitively large amount of telescope time. Second, stellar kinematics cannot be uniquely mapped to a given potential; there are different sets of orbits resulting in the same observed surface mass distribution and kinematics. Thus, despite its apparent shortcomings H II measurements seem to be the most promising method with which to approach the problem.

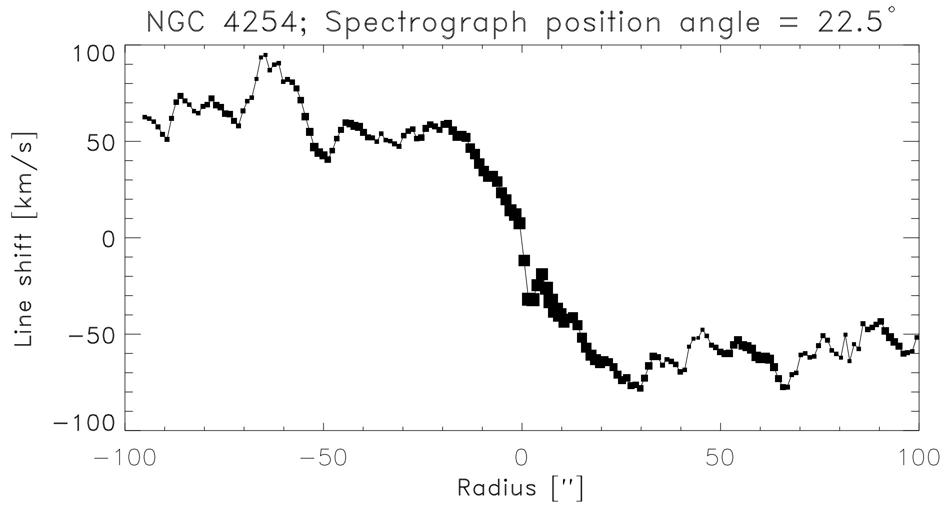

Figure 5.10 NGC 4254 rotation curve for the slit position angle of 22.°5. The plot symbol sizes reflect the intensity of the Hα-line at each radius. It is apparent that stong wiggles are not directly related to single H II regions.

Could the discrepancies between modelled and observed kinematics be related to taking the NIR K-band image of a galaxy as the basis to calculate its stellar potential? As already discussed in Section 4.1.2 there are several factors which throw into question whether the K-band image is a good constant mass-to-light ratio map of the stellar mass distribution despite the color correction we applied. However, the two major factors – population effects and dust extinction – tend to affect the arm-interarm contrast, rather than the location of the K-light spiral arms. Dust lanes lie preferentially inside the $m = 2$ component of a galaxy's spiral (Grosbøl, Block & Patsis 2000) absorbing interarm light, while the red super giants may actually have their highest density in the spiral arms directly, where they emerged from the fastest evolving OB stars. This effect should become apparent in the simulations as slightly wrong amplitudes of the gas wiggles, leaving their radial position mostly unchanged. So even if the K-band images might actually include unaccounted mass-to-light ratio variations, they most probably introduce only small errors, which should not result in an overall mismatch of the models with the data. The color-corrected K-band images should therefore reflect the stellar mass accurately enough for our analysis. Certainly, there appears to be no better practical mass estimate that we could use for our analysis.

5.3.2. Are there Systematic Errors in the Modelling?

The most critical part of this study are the several modelling steps required to predict the gas velocity field for the comparison with the data. We apply a spatial filter to the K-band image before calculating the disk potential to reduce the significance of the clumpy H II regions (as described in Section 4.1.4). The residual map of the discarded component shows all the bright H II regions in the disk, giving us confidence that we have excluded much of the structures that reflect small-scale M/L variations. This correction removes roughly 3.5 % of the total K-band light and does not depend strongly on the number of Fourier components used for the fit. For two extreme decompositions employing 6 and 16 Fourier components, the mean resulting relative discrepancy in the derived potentials is only $\approx 10^{-6}$. One remaining concern in calculating the potential might be that the mass density map cuts at the border of the image. However, the galaxy completely fits in the frame, fading into noise before the image border. Moreover, we do not perform the simulations for the complete galaxy, but only for the inner 11.6 kpc in radius. So the edge cutoff effect is very small and affects the part of the potential we are looking at even less.

For the dark matter component we chose an isothermal halo with a core because of its flexibility in fitting rotation curves. The functional form of the dark halo profile has only a second order effect on the results of the simulations compared to the variations due to its two basic parameters R_c and v_∞. We decided not to distinguish between different dark halo profiles for the present analysis.

The most complex step surely is the hydrodynamical simulation of the gas flow in the galaxy's potential. Beyond the tests of the code discussed in Section 4.2.2, it is the excellent morphological agreement between the simulated gas density profiles and the observed spiral arms that gives credence to the results of the code. However, for NGC 4254 and other galaxies whose inclination with respect to the line-of-sight is relatively low, shortcomings in the kinematics comparison may arise from the two dimensional nature of the simulations. While in such cases the observations are rather sensitve to gas motions perpendicular to the plane of the disk, those velocity components cannot be modelled. This is certainly a systematic error that must be kept in mind.

In a real galaxy the assumption of a global constant pattern rotation speed may not be fulfilled. In particular, we should expect the central bar to have a different pattern speed. Also, the pattern might be winding slowly, rather than being fixed in a corotating frame. Furthermore, the gas may not have a uniform temperature. If these simplifications were relaxed, the location of the spiral arms in the hydro-simulations would change, and eventually lead to a different overall fit quality. Lacking any solid basis to constrain these parameters, we are unable to implement these effects into the modelling procedure. Finally, the code does not include gas self-gravity. The effect of gas self-gravity is difficult to quantify without actually performing simulations, but from the literature we know that it tends to amplify the gas response. Gas self-gravity also suppresses the tendency of the gas to shock (Lubow, Balbus & Cowie 1986). Since we are interested in the strength of the gas response to the gravitational potential and we already find that for high disk M/L the response is too strong, we assume that our upper limit holds also if gas self-gravity was included. Given the good morphological match, we may confidently assume that all our approximations are not far off.

This leaves non-gravitationally induced gas motions and the fact that any gas motion perpendicular to the plane of the disk cannot be reproduced by two dimensional gas simulations as the main complications in the comparison of the models to the observed kinematics. Eliminating mismatching wiggles from the rotation curve is not possible since we have no means to reliably identify the ones that are non-gravitationally induced. Any method we apply to excluding parts of the data will be affected by some kind of bias[2].

[2] The method that was described in Section 4.3.2.1 was developed after this paper have been published.

5.3.3. Is the Galaxy Suited for this Analysis?

Finally we must consider the possibility that the galaxy we picked for our analysis might not be as suited as it appeared to be. NGC 4254 is not the prototype of a classical grand design spiral galaxy in optical wavelengths. However, as it can be seen in the central frame of Figure 5.2, the galaxy exhibits in the M/L corrected K'-band image mainly an $m = 2$ spiral pattern with a strong symmetric part, that ends at ≈ 5.5 kpc and fainter outer extensions. With its large angular size and moderate inclination, NGC 4254 seems to be one of the most promising candidates for this kind of study in our sample. However, as discussed in the first paragraph of this Chapter, there are indications that this galaxy might not be as isolated and undisturbed as one might expect. In fact, the morphology itself implies some perturbative event in its recent evolution history: NGC 4254 shows a clear $m = 1$ mode and a lopsided disk. In this respect it was argued earlier that in-falling H I gas clumps, which are visible in radio data and do not emit in Hα, might be responsible for triggering deviations from pure grand design structure (Phookun et al. 1993). So have we reason to believe that NGC 4254 is far from equilibrium? This is hard to tell, because on the other hand we find plenty of arguments that a stable propagating density wave in NGC 4254 is responsible for its morphology. This galaxy shows many similarities to the spiral galaxy NGC 5247 whose morphological and dynamical properties were discussed by Patsis, Grosbøl & Hiotelis (1997), based on SPH simulations. We note that in our best model, the strong bisymmetric part of the K' spiral, ends well inside the corotation radius, although fainter extensions reach out to it. This picture is in agreement with the 4/1 SPH models of Patsis et al. (1997). Assuming corotation close to the characteristic bifurcation of the arms at ≈ 5 kpc on the other hand, we do not obtain satisfactory results (upper left frame in Figure 5.2). Based on this is seems appropriate to conclude that NGC 4254 is at least close to an equilibrium state and it should be suited for a case study.

5.4. Conclusions

We performed hydrodynamical simulations to predict the gas velocity field in a variety of potentials for the spiral galaxy NGC 4254 and compared them to observations. These potentials consisted of different combinations of luminous (non-axisymmetric spiral) and dark matter (axisymmetric) components. The resulting gas spiral morphology reflects very accurately the morphology of the galaxy and allows us to specify the corotation radius or the pattern speed of the spiral structure quite precisely. It is noteworthy that within the error range given, the best matching pattern speed does not depend on the mass fraction of the stellar disk relative to the dark halo. For NGC 4254 we find that the corotation lies at 7.5 ± 1.1 kpc, or at about 2.1 exponential K'-band disk scale lengths. From the kinematics of the gas simulations we could rule out a maximal disk solution for NGC 4254. Within the half-light radius the dark matter halo still has a non-negligible influence on the dynamics of NGC 4254: specifically, our fraction $f_d \lesssim 0.85$ implies that $\gtrsim 1/3$ of the total mass within 2.2 K-band disk scale lengths is dark. However, the comparison of the simulated gas velocity field to the observed rotation curves turned out to be a delicate matter. The observed rotation curves show a significant number of bumps and wiggles, presumably resulting from non-gravitational gas effects, that complicate the identification of wiggles induced by the massive spiral arms. Therefore, beyond concluding that the disk is less than 85 % of maximal, we were unable to specify a particular value for the disk mass or to test the results from Bottema (1997) or Courteau & Rix (1999). But already with this statement we differ from the conclusions of Debattista & Sellwood (2000) and Weiner et al. (2001b), who argue that their conclusions for maximal disks of barred galaxies also hold for non-barred spirals. Since we only analyzed one galaxy so far it is inappropriate to state here that the centers of unbarred spirals, what we still consider NGC 4254 to be despite its small bar-like structure in the very center, are generally governed by dark matter.

In the next Chapter the results from more galaxies are presented. This will create a broader basis to decide, whether single galaxies differ very much in their dark matter content, or if the bulk of the spirals show similar characteristics.